Diacylglycerol-dependent hexamers of the SNARE-assembling chaperone Munc13-1 cooperatively bind vesicles

Feng Li, Kirill Grushin, Jeff Coleman, Frederic Pincet, James Rothman

Diacylglycerol-dependent hexamers of the SNARE-assembling chaperone Munc13-1 cooperatively bind vesicles

Feng Li[1,2], Kirill Grushin[1,2], Jeff Coleman[1,2], Frederic Pincet[1,2,3,*], and James E. Rothman[1,2,*]

[1]Department of Cell Biology, School of Medicine, Yale University, 333 Cedar Street, New Haven, CT 06520, USA

[2]Nanobiology Institute, Yale School of Medicine, West Haven, CT 06516, USA

[3]Laboratoire de Physique de l'Ecole normale supérieure, ENS, Université PSL, CNRS, Sorbonne Université, Université de Paris, F-75005 Paris, France

* Correspondence to James E. Rothman or Frederic Pincet

Email: james.rothman@yale.edu, frederic.pincet@ens.fr

Keywords: Munc13-1, cluster, SNARE, Syntaxin, synaptic vesicle, neurotransmission, membrane fusion, TIRF, diacylglycerol, $PI(4,5)P_2$

ABSTRACT

Munc13-1 is essential for vesicle docking and fusion at the active zone of synapses. Here we report that Munc13-1 self-assembles into molecular clusters within diacylglycerol (DAG)-rich microdomains present in phospholipid bilayers. Although the copy number of Munc13-1 molecules in these clusters has a broad distribution, a systematic Poisson analysis shows that this is most likely the result of two molecular species: monomers and mainly hexameric oligomers. Each oligomer is able to capture one vesicle independently. Hexamers have also been observed in crystals of Munc13-1 that form between opposed phospholipid bilayers (*1*). Mutations targeting the contacts stabilizing the crystallographic hexagons also disrupt the isolated hexamers, suggesting they are identical. Additionally, these mutations also convert vesicle binding from a cooperative to progressive mode. Our study provides an independent approach showing that Munc13-1 can form mainly hexamers on lipid bilayers each capable of vesicle capture.

SIGNIFICANCE STATEMENT

Munc13-1 is a molecular chaperon that facilitates recruitment and docking of synaptic vesicles at the active zone of the synapse. Using model membranes and statistical modeling, we show that Munc13-1 forms mainly hexamers on diacyl-glycerol rich microdomains on lipid membranes. These hexamers act cooperatively to capture vesicles from a solution. Statistics show that each hexamer binds to one vesicle. Disruption of the interactions at Munc13-1 hexagonal interface by point mutations based on crystallographic data alters its oligomerization state and hexamers are no longer observed. Furthermore, the mutant oligomer loses its cooperativity in binding vesicles. Our study suggests that the Munc13-1 hexamers observed on lipid bilayers resemble the hexagons revealed by crystallography.

INTRODUCTION

Many cellular proteins form oligomeric structures to achieve their specific biological functions (*2-4*). Numerous proteins required for neurotransmitter release are concentrated within the crowded active zones of presynaptic terminals, potentially favoring the assembly of well-defined oligomeric structures that would not be observed in dilute solution. Relatively small differences in energy amongst a series of alternative oligomeric arrangements could then enable successive rearrangements to occur in a defined order, thereby choreographing the process of vesicle capture and activation for fusion. In this paper we will report novel properties of oligomers of the synaptic protein Munc13-1 which assemble on lipid bilayers following concentration within diacylglycerol (DAG)-rich microdomains likely mimicking portions of the pre-synaptic active zone.

Munc13-1 is a key chaperone protein required for the assembly of the SNARE complex of Syntaxin1, VAMP2, and SNAP25 which ultimately triggers membrane fusion for synaptic transmission (*5-15*). Munc13-1 is a large molecule, the C-terminal half of which contains its characteristic MUN domain, flanked at one end by a DAG-binding C_1 domain and a PIP_2 and Ca^{++} - binding C_2B domain, and at the other end by its phosphatidyl-serine (PS)-binding C_2C domain. Munc13-1 is initially required to capture synaptic vesicles via its C_2C domain (*16, 17*), it is later required to activate Syntaxin1 to initiate SNAREpin assembly (*18*) during which it interacts with each of the three synaptic SNARE proteins (*18-20*), and approximately 5-10 copies remain in close association with each primed, ready-release vesicle (*21, 22*) most likely containing 6 clamped central SNAREpins arranged symmetrically on a ring (*23, 24*). Munc13-1 is therefore ideally positioned to choreograph this entire process via a series of oligomeric assemblies.

We previously reported that purified Munc13-1 protein reconstituted onto supported lipid bilayers containing DAG and PIP_2 is organized into clusters containing from 2 to ~20 copies, as revealed by a combination of quantitative Total Internal Reflection Fluorescence (TIRF) microscopy and stepwise photobleaching (*17*). We noted that only clusters containing a minimum of 6 copies of Munc13-1 were capable of efficiently capturing and retaining PS-containing small unilamellar vesicles (SUVs). This hinted that a hexamer of Munc13 could be a basic functional unit for vesicle binding, a conclusion that had no structural precedent at the time.

Direct evidence for a hexameric organization then emerged when we solved the structure of two-dimensional crystals of Munc13-1 that spontaneously assemble between bilayers containing copious acidic phospholipids, revealing two novel oligomeric arrangements: a 21 nm high 'upright' trimer that binds both bilayers, and a 14 nm high 'lateral' hexagon (*1*). The hexameric structure of Munc13-1 is particularly of interest because it may represent a fusion intermediate, with six Munc13-1 dependent protein complexes under each closely docked synaptic vesicle, which is consistent with the electron tomography studies which showed that the protein density between synaptic vesicles and the plasma membrane exhibited 6-fold symmetry (*23, 24*).

The straightforward interpretation of these results (*1*) is that upright trimers first capture synaptic vesicles by PS-dependent binding to their plasma membrane-distal C_2C domains and then transition closer to the plasma membrane as the trimers re-arrange to form hexamers. However, this model would seem to require that the top surface of the hexamer retains the synaptic vesicles, even though the known vesicle binding surface in C_2C is sterically unavailable in the hexamer (*1*). The structural model (*1*) and *in vitro & in vivo* functional assays (*25, 26*) also strongly predicted that DAG binding by the C_1 domain should trigger the rearrangement of trimers into hexamers, which involves a simple intra-molecular rigid body rotation of C_1-MUN-C_2C relative to C_2B, which remains fixed on the plasma membrane surface (*1*). This followed because the DAG binding site is closely opposed to the bilayer surface in the hexamer but points away from the bilayer in the trimer.

In this study we have built on the observation that clusters of approximately 6 copies of Munc13 bind a vesicle (*17*) to test these predictions. Specifically, we now investigate whether isolated hexamers of Munc13 can form on lipid bilayers, whether they require DAG to assemble, and whether each hexamer can potentially retain synaptic vesicles following their initial capture by upright trimers.

RESULTS AND DISCUSSION

DAG forms microdomains within phospholipid bilayers

Diacylglycerol (DAG) is a lipid in plasma membrane at relatively low concentration. However, the membrane lipid phosphatidylinositol 4,5-bisphosphate ($PI(4,5)P_2$) is known to form clustered

104 domain in lipid bilayers in the presence of Syntaxin-1 juxtamembrane domain (*27*).
105 Consequently, DAG may exist in the form of clustered microdomains when such enriched
106 PI(4,5)P_2 is hydrolyzed to DAG by the phospholipase C (*28-30*). DAG has been reported to
107 induce phase transition in phospholipid bilayers (*31*). Molecular dynamics simulations suggest
108 that DAG may form domains in the bilayers (*32*). Hence, such DAG domains may have been
109 present in our previous study on Munc13-dependent vesicle binding (*17*). To test this directly,
110 we examined the distribution of a fluorescently labelled analogue of DAG, TopFluor® DAG
111 (*33*), replacing ordinary DAG (2 mole%) in bilayers also comprised of 71 mole% PC, 25% PS,
112 and 2% PI(4,5)P_2, the same composition used in our previous study (see Materials and Methods
113 for acronyms). Fig. 1A (left panel) confirms that micro-domains of DAG were indeed present.
114 These DAG-rich domains ranged in area from less than 0.5 μm^2 up to about 2 μm^2, averaging 0.7
115 $\pm$ 0.5 μm^2 for 2 mole% total DAG (Fig. 1F, red bars). Higher concentrations of DAG, tested up
116 to a total of 10 mole% total (2 mole% TopFluor® DAG analogue with the balance of DAG being
117 underivatized DAG) resulted in somewhat larger microdomains, the largest being 2 – 3 μm^2 at
118 10% total DAG (Fig. 1F). The average DAG domain was 0.8 $\pm$ 0.7 μm^2 at 5 mole% total DAG
119 and 1.2 $\pm$ 0.8 μm^2 at 10 mole% total DAG.

120

121 **Munc13-1 binds preferentially to the DAG microdomains**

122 We next tested whether Munc13-1, previously shown (*17*) to bind to DAG-containing bilayers in
123 clustered regions that could not be resolved optically, might be selectively localized within DAG
124 domains. For this purpose, we employed a minimal fragment of Munc13-1 known to be
125 functional *in vivo* (*10, 20*), consisting of C_1-C_2B-MUN-C_2C (residues 529 to 1735; Munc13C)
126 with a Halo domain added at its C-terminus (Munc13C-Halo). This protein was rendered
127 fluorescent by reacting the Halo tag with Alexa Fluor 660 ligand. The theoretical molecular
128 weight of this protein is 167 kDa. It is soluble in buffer solution. In mass photometry
129 measurements, it displayed a large peak at 169 $\pm$ 15 kDa, and a barely noticeable second peak at
130 329 $\pm$ 21 kDa (Fig. 1G). This confirmed that the starting material in our experiments, 10 nM
131 Munc13-1 in solution, was primarily momomeric with an extremely small fraction of dimers.

132

We incubated the supported lipid bilayer with such 10 nM Munc13-1 solution. Then we simultaneously imaged DAG (TopFluor®, 488 nm) and Munc13C (Alexa 660) on the lipid bilayer by TIRF.

Fig. 1A-C (middle panels) reproduces our original finding that Munc13C forms clusters and goes on to present new data that establishes that at 2 – 10 mole% DAG almost all of these Munc13-1 clusters are within the DAG microdomains (Fig. 1A-C, panels at right). This suggests that DAG locally increases its own concentration through self-aggregation, resulting in DAG microdomains which recruit and locally concentrate Munc13C molecules.

The number of copies of Munc13C in each DAG domain was then determined by a combination of quantifying the TIRF intensity and stepwise photobleaching as before ((*17*), Material and Methods). The frequency distributions of copy numbers were indistinguishable at 2 mole% (red) and 5 mole% (blue) DAG, and the same whether the DAG was fluorescently tagged (red) or natural DAG (dashed line), showing that Munc13-1 binding is not affected by the fluorescent probe. Very little binding or clustering of Munc13-1 occurred when DAG was omitted from the bilayers (Supporting Fig. S1).

Because Munc13-1 can potentially bind to the plasma membrane either to $PI(4,5)P_2$ (via C_2B) or to DAG (via C_1) or to both lipids simultaneously, it was of special interest to determine whether $PI(4,5)P_2$ is excluded from the DAG microdomains. For this purpose we prepared bilayers containing 2 mole% non-fluorescent DAG and 2 mole% TopFluor® $PI(4,5)P_2$. We observed that $PI(4,5)P_2$ was nearly uniformly distributed in the lipid bilayer and Munc13-1 clusters were formed in $PI(4,5)P_2$ region (Fig. 1D), which suggested that $PI(4,5)P_2$ was neither concentrated within nor excluded from the DAG microdomains. This implies that Munc13-1 bound to DAG microdomains can potentially be bound to both DAG and $PI(4,5)P_2$ simultaneously.

Mass Photometry experiments showed Munc13-1 remained as monomer in solution, from 8 nM to 170 nM, (Supporting Fig. S2). This result indicates that DAG, in addition to locally increasing the Munc13-1 concentration, also provides a binding interface for correctly orientating Munc13-1 for oligomer formation, as already suggested by the previous cryo-electron tomography study.

Poisson distribution analysis reveals that Munc13-1 assembles into discrete oligomers within DAG microdomains, most likely hexamers

As reported previously (*17*), we are able to determine the number of Munc13-1 molecules, *N*, in each cluster. For a given cluster, in principle such *N* Munc13-1 molecules may exist in the form of monomers or oligomers, or a combination of these states. The likelihood of lateral diffusion of the Munc13-1 molecules within the clusters makes it difficult to determine their oligomeric state from optical microscopy alone, and this difficulty is compounded when the domains are close in size to the wave length of the light. For example, a "cluster" with a copy number of 6 Munc13-1 molecules ($N = 6$) could be at one extreme 6 individual, non-interacting monomers diffusing freely over the surface of a common lipid microdomain, or at the other extreme a rigidly structured hexamer such as is observed bound to bilayers in the Munc13-1 crystal (*1*).

To rule out the trivial explanation (null hypothesis) that the observed Munc13-1 clusters are merely a collection of individual proteins that happen to be bound to the same lipid microdomain we can employ well-understood Poisson statistics to analyze the copy number distribution of the apparent Munc13-1 clusters. In the null hypothesis the frequency distribution of copy numbers will be given by:

$$P_M(m) = \frac{\langle m \rangle^m}{m!} e^{-\langle m \rangle} \qquad (1)$$

Where m is the number of monomers and $\langle m \rangle$ the mean copy number of Munc13-1 molecules per cluster. $\langle m \rangle$ cannot be directly measured experimentally since the domains without any Munc13-1, *i.e.*, $P_M(0)$, is unknown because in most experiments we used unlabeled DAG. Hence, the observed copy number probability needs to be corrected for it. This is a straightforward process (see Supporting text). This model assumes that the DAG microdomains are of uniform size which is reasonable considering the measured area distribution. With these considerations, we determined that $\langle m \rangle \approx 4.8$ copies of Munc13-1 per cluster at 2 mole% total DAG. This predicts a copy number distribution (Fig. 2A, bars) that clearly does not match with the observed distribution (dashed line). We can conclude that the null hypothesis is incorrect. That is, the observed copy number distribution can only be explained by molecular interaction amongst the bound Munc13-1 into stable oligomers which distribute as such amongst the individual cluster.

We can further refine the statistical model to provide deeper insight into the degree of oligomerization of Munc13-1 that is likely involved, which we term '*K*'. For example, if monomers were to assemble exclusively into hexamers, then $K = 6$, and a cluster containing 8 copies of Munc13-1 ($N = 8$) would in fact most likely contain 1 copy of a hexamer and 2 unassembled monomers or, less likely, 8 copies of individual Munc13-1. More generally, we will determine the best fit for *K* to the experimental data with the assumption that Munc13-1 is present in clusters only as combinations of monomers and *K*-mers. These two populations behave independently of each other and each randomly distributes amongst clusters following its own Poisson probability distribution, exactly as in the first model:

$$P_M(m) = \frac{\langle m \rangle^m}{m!} e^{-\langle m \rangle}$$
$$P_K(k) = \frac{\langle k \rangle^k}{k!} e^{-\langle k \rangle} \quad (2)$$

where P_M and P_K are the probability distributions for monomers and *K*-mers, respectively, and m and k are respectively the numbers of copies of monomers and *K*-mers in the cluster.

The observed copy number distributions of Munc13 cluster result from combining the monomers and *K*-mer distributions, as presented in Supporting Table S1. $\langle m \rangle$ and $\langle k \rangle$ can then be calculated (see Supporting text for explanations). The predicted probability distribution of copy numbers is fully described by these two parameters (Eq. S5 in the supporting information).

The resulting copy number distributions predicted from dimer to decamer, $K = 2$ to $K = 10$, are shown in Figure 2B-D and Supporting Figure S3. The predicted distribution for hexamers ($K = 6$) closely matches the experimental results (dashed lines). In particular, this model correctly predicts the second peak at $N = 8$ and the third peak at $N = 14$. Flanking models ($K = 5$ and $K = 7$) do not predict these observed peaks. To objectively assess which model(s) seems to describe best the observed cluster size distribution, we use a parameter to test the oligomerization degree, *O*, that quantitatively compares the predicted and observed histograms for each *K*-mer. A larger *O* value indicates a better prediction of the experimental distribution. The results confirm that the hexamer model has the highest *O* value (Fig. 2E and Supporting text).

Finally, another prediction from this model is that the fraction of DAG domains without any Munc13-1 is:

$$P_{Total}(0) = e^{-\langle k \rangle} e^{-\langle m \rangle} \quad (3)$$

In the case of hexamers, $\langle m \rangle = 2.4$ and $\langle k \rangle = 0.375$ which leads to $P_{Total}(0) = 0.06 = 6\%$. Experimentally, we can estimate $P_{Total}(0)$ from experiments with bilayers containing fluorescent DAG. We find 9 ± 2% of DAG domains lack Munc13C, which is reasonably close to the predicted value considering the simplicity of our model.

Targeted mutations predicted to destabilize the hexamers observed in crystals alter the Munc13-1 copy number distribution and disrupts co-operative vesicle binding

Are the predominantly hexameric units of Munc13-1 that assemble in clusters on the surface of single lipid bilayers structurally equivalent to the Lateral Hexagons that assemble in protein crystals between bilayers (*1*)? The Lateral Hexamer assembles when the Munc13-1 molecules are in their 'closed' conformation and when the C_2C domain of one copy contacts the MUN domain of its neighbor. This geometry results in a closed hexameric ring (Fig. 3A).

It was previously shown by cryo-electron tomography that Munc13-1 forms hexagonal lattice between negatively charged lipid bilayers (*1*). We located possible interacting amino acid within the lateral interfaces between C_2C domain and MUN domain of neighbor molecule in the hexagonal formation of Munc13-1 (Fig. 3A). This interface was proposed to consist of two regions – hydrophobic (a/a F1176 and I1215 on MUN domain and corresponding interaction partners W1626 and W1684 on C_2C domain) and polar (a/a E1139 and D1039 on MUN domain and R1678, R1673 on C_2C domain) (Fig. 3B). These two regions are well conserved in vertebrates and the hydrophobic region is conserved in invertebrates as well (Supporting Figure S4).

To test selected amino acid residues, we mutated them on MUN domain to N1176, N1215, R1139 and R1039. We refrained from mutating the corresponding residues on C_2C domain due to possible negative effect on membrane binding abilities. This quadruple mutation not only disrupted the formation of the hexagonal crystal but also led to the assembly of a new rectangular crystal lattice (Fig. 3D and Supporting Figure S5). Visually protein packing is much denser than wild-type with visible rows of round-shaped protein densities and diagonally placed proteins connections between them (Figs. 3C and 3D). When measured between the centers of round elements, rows are spaced by 35 nm, and round elements within a row are spaced by 12 nm. Distance between bilayers, as measured on the side views (Figs. 3C and 3D) is similar and ~21

nm suggesting the presence of upright open configuration of the protein in the new crystal. The 3D reconstruction of a new crystal is ongoing and will hopefully show the details of a new crystal assembly.

If the oligomers assembling on Munc13-1 clusters on lipid bilayers are in fact Lateral Hexagons in the cryo-electron tomography study, they too should be disrupted by these mutations. To test this, we used the same mutant version of Munc13C as above, F1176N, I1215N, E1139R, and D1039R, and measured its copy number distribution and vesicle capture property (Fig. 3E). The mutant bound to DAG-containing lipid bilayers and formed cluster, similar to the wild-type protein, but had a markedly reduced copy number distribution (Fig. 3F). In particular, the predicted peaks for hexamers at $N = 8$ and $N = 14$ are abolished. Instead, a new peak is observed at $N = 5$. Applying the same model and methodology as for the Poisson analysis of the wild-type protein (Eq. 2 and Supporting Eq. S5) reveals that only a tetramer ($K = 4$) model predicts the new peak at N = 5 (Supporting Fig. S6), and that a tetramer has by far the largest O value (Fig. 3G). Further work involving direct structure determination will be required to independently confirm this conclusion.

In any case, the new results imply that C_2C is required for the observed hexameric clustering of Munc13C. Our previous report we suggested that C_2C could be deleted without affecting clustering (Fig. 4B in ref. (*17*)). With the perspective of the current work, re-examination reveals that clustering without C_2C results in smaller clusters and the distribution notably differs from that of wild-type especially at copy numbers of 6 and 12, suggesting that there is a C_2C-independent non-hexameric form of clustering that can occur when C_2C is artificially removed.

We previously reported that Munc13-1 clusters formed on DAG-containing lipid bilayers bound PS-containing SUVs depending on the number of copies of Munc13-1 present (*17*). In particular, we found that clusters containing 6 or more copies of Munc13-1 always captured a vesicle, and those with 4 or fewer copies almost never did, suggesting that 6 copies of Munc13-1 optimally co-operate to capture a vesicle when Munc13-1 was bound to DAG via its C_1 domain, as disrupting the interaction between DAG and C_1 reduced recruitment of Munc13-1 (Supporting Fig. S7), while $PI(4,5)_2$ has a partial contribution to the recruitment but little effect on the size distribution of the clusters (Supporting Fig. S8). We have confirmed and extended these data in

Fig. 4, which now tests the important prediction that vesicle binding, relying as it does, on Munc13-1 binding should likewise be DAG-dependent (compare Figs 4A and B, with and without DAG, respectively). Comparing the Munc13-1 copy number content of those clusters which fail to capture a vesicle (Fig. 4C, blue bars) with those that do (orange bars) confirms that it is only when the cluster contains 6 or more copies that it does not fail to capture a vesicle. This is also true for Munc13-1 clusters on the bilayer in the absence of DAG, where there is barely any co-localization with captured vesicles because the copy numbers of Munc13-1 molecules in these clusters are usually less than 6 (Fig. 4D).

These experiments cannot in and of themselves distinguish whether the 6 co-operating copies of Munc13-1 are pre-assembled into a hexamer as distinct from assembling around a vesicle during the process of capturing it. However, the former model makes a unique prediction, that disrupting the hexamers should eliminate the co-operativity of vesicle binding. To test this, fluorescent vesicles containing 68 mole% PC, 30% PS and 2% PE-Atto647N were incubated with supported lipid bilayers harboring the Munc13-1 quadruple mutant (F1176N I1215N E1139R and D1039R) clusters. The bilayers were then washed to remove unbound vesicles and imaged using TIRF microscopy (Fig. 3E, three panels at top). The results were quantified by measuring the number of copies of the Munc13-1 mutant in each cluster and scoring that cluster for the presence or absence of vesicles (Fig. 3H). As predicted for co-operative vesicle binding to hexamers, the hexamer-destabilizing mutations (purple bars) reduced the probability of vesicle capture at $N = 6$, the threshold observed for co-operative binding by the wild-type protein (Fig. 3H, green dashed line, reproduced from ref. (*17*)).

As strikingly, co-operativity was eliminated. Vesicle capture by the mutant increases progressively (nearly linearly) with the number of copies present. This suggests that each copy of the mutant, unable to form hexamers, now binds to vesicles independently.

Each hexamer appears to capture a single vesicle

So far, we have not attempted to distinguish the number of vesicles bound to each Munc13-1 cluster. Two vesicles bound to the same cluster would be difficult or impossible to resolve optically. However, the fluorescent intensities of these vesicles would be additive. With this in mind, we measured the total vesicle fluorescence intensity colocalizing with each Munc13-1

cluster and related it to the number of copies of Munc13-1 bound to the same cluster (Fig. 5A and B). There is a clear increase in vesicle intensity with the copy number of Munc13-1 molecules in the cluster (Fig. 5C).

The simplest model would be that each hexamer can bind one vesicle. If this were the case, we would observe a quantal rather than a progressive increase in the number of vesicles bound as a function of copy number. In particular, these steps should occur around $N > 8$ and $N > 14$, where one and two hexamers predominate (Fig. 2C). In fact, this is exactly what we observe (Fig. 5C).

Because the size of each vesicle (and thus its intensity) follows a probability distribution, it is not necessarily straightforward to relate the intensities in each step to the number of vesicles, even though the vesicles in the capture experiments have a narrow size distribution with a mean radius of ~31 ± 9 nm (Supporting Fig. S9). However, this can be done with a normalization process that takes into account the various combinations of monomers and hexamers that can combinatorially result in a given copy number for a cluster (see Table S1) and their associated probabilities for vesicle binding. As a result, we can calculate the mean number of vesicles bound to a cluster as a function of its overall copy number as predicted by the quantal binding model (Fig. 5D). The good agreement between the predictions and observations suggests that our assumptions are correct and that each DAG-dependent hexamer captures a single vesicle as an independent co-operative unit.

CONCLUDING REMARKS

In summary, a combination of biochemical and structure-based mutation data imply that hexamers corresponding to the lateral hexamers in protein-bilayer crystals (*1*) form as stand-alone structures on DAG-rich microdomains (Figs. 1-3); that hexamer assembly depends on binding to DAG microdomains (Fig. S1C); and that each hexamer co-operatively captures a single vesicle (Fig. 5). Therefore, hexamers are predicted to bind two bilayers simultaneously. It will be important to directly visualize such structures by cryo-electron microscopy in future studies.

Our conclusion that hexamers can still bind vesicles is satisfying biologically because it would explain how a synaptic vesicle captured initially by the C_2C domains of upright trimers of

Munc13-1 (21 nm high) could be retained at the plasma membrane after these trimers have putatively transitioned into hexamers (now 14 nm high) as Munc13-1 transitions from its open to closed conformation, putatively driven by DAG binding. Yet, this conclusion is also surprising from a structural perspective. The upright trimers bind bilayers representing the vesicle by their C_2C domains, and our cryo-EM structure (*1*) directly visualized the surface of C_2C that would be in contact with a synaptic vesicle. But as we have detailed (*1*) in the closed conformation of the subunits of a hexamer, this very surface of C_2C is engaged in binding to the neighboring MUN domain and thus sterically unavailable.

Presumably a new surface is created on the top of the hexamer that contains a combination of hydrophobic and basic residues which can multivalently bind negatively charged PS-containing phospholipid vesicles (*17*). It remains for future work to identify the constituents of this unanticipated vesicle binding surface.

Moreover, our work suggest that oligomerization of synaptic proteins is a critical form of organization at the presynaptic membrane. Many important tethers in synaptic fusion, such as the RIM protein, RIM-BP, and Synapsin, are known to undergo phase separation and form condensed liquid droplets in the active zone (*34, 35*). These droplets are a form of oligomerization. These findings show that oligomerization occurs quite often, and is probably a general mechanism for locally obtaining high concentration.

MATERIALS AND METHODS

Chemicals. 4-(2-Hydroxyethyl)piperazine-1-ethanesulfonic acid (HEPES), Potassium hydroxide (KOH), Potassium chloride (KCl), Magnesium chloride ($MgCl_2$), Glycerol, DNAse I, RNAse A, Benzonase, Roche complete protease inhibitor cocktail tablets, Phorbol 12-myristate 13-acetate (PMA), and DL-Dithiothreitol (DTT) were purchased from Sigma-Aldrich. Nickel-NTA agarose, TCEP-HCl, and Expi293™ Expression System Kit were supplied by Thermo Fisher Scientific. The lipids used in this study, 1,2-dioleoyl-sn-glycero-3-phosphocholine (DOPC), 1-palmitoyl-2-oleoyl-sn-glycero-3-phosphocholine (POPC), 1,2-dioleoyl-sn-glycero-3-(phospho-L-serine) (sodium salt) (DOPS), L-α-phosphatidylinositol-4,5-bisphosphate (Brain, Porcine) (ammonium salt) (brain $PI(4,5)P_2$), 1-2-dioleoyl-sn-glycerol (DAG), 1,2-dioleoyl-sn-glycero-3-phosphoethanolamine-N-(7-nitro-2-1,3-benzoxadiazol-4-yl) (ammonium salt) (DOPE-NBD), 1-

palmitoyl-2-(dipyrrometheneboron difluoride)undecanoyl-sn-glycerol (TopFluor® DAG), 1-oleoyl-2-{6-[4-(dipyrrometheneboron difluoride)butanoyl]amino}hexanoyl-sn-glycero-3-phosphoinositol-4,5-bisphosphate (ammonium salt) (TopFluor® PI(4,5)P_2), and 1-oleoyl-2-(6-((4,4-difluoro-1,3-dimethyl-5-(4-methoxyphenyl)-4-bora-3a,4a-diaza-s-indacene-2-propionyl)amino)hexanoyl)-sn-glycero-3-phosphoinositol-4.5-bisphosphate (ammonium salt) (TopFluor® TMR PI(4,5)P_2) were purchased from Avanti Polar Lipids. 1,2-Dioleoyl-sn-gylcero-3-phosphoethanolamine ATTO 647N (DOPE-Atto647N) was from ATTO-Tec. The plasmid maxi prep kit was from QIAGEN. HaloTag® Alexa Fluor® 488 Ligand and HaloTag® Alexa Fluor® 660 Ligand were purchased from Promega. All aqueous solutions were prepared using 18.2 MΩ ultra-pure water (purified with the Millipore MilliQ system).

Protein constructs, expression and purification.

The original vector expressing rat Munc13 was a kind gift from Dr. Claudio Giraudo. Similar to our previous report (*17*), the expression plasmids His_{12}_PreScission _C_1_C_2B_MUN_C_2C_tev_Halo and His_{12}_PreScission _C_1_C_2B_MUN_C_2C_tev_Halo quadruple mutant (F1176N I1215N E1139R D1039R), were produced by cloning rat Munc13-1 residues 529 to 1735, respectively, to a pCMV-AN6 plasmid. Munc13-1 residues 1408-1452 were deleted and residues EF were added in their place (*36*). A short linker sequence containing a TEV cut site was subcloned in followed by the Halo tag. For CryoET studies, the cDNA construct with His_{12}–Munc13C (Munc13-1 residues 529 to 1735 with residues 1408 to 1452 replaced by the sequence EF) was expressed in a modified pCMV–AN6 vector, which includes a PreScission cut site following the His12 tag. The quadruple mutant (F1176N/I1215N/E1139R/D1039R) was generated using a QuickChange mutagenesis kit (Agilent Technologies).

The resulting plasmids were amplified with maxi prep using QIAGEN Plasmid Maxi kit and were used to transfect Expi293F™ human cells. Proteins were expressed with Expi293™ expression system following the manufacturer's protocol.

The Munc13-1 proteins were then purified using Ni-NTA affinity beads as described before (*37-39*). To summarize, the cell pellet was thawed on ice and disrupted with a homogenizer, and then spun in an ultracentrifuge for 30 minutes at ~142,400xg at 4°C. The supernatant was removed and 2 mL Qiagen Ni-NTA slurry along with 10 uL Benzonase were added, and subsequently

rotated using an orbiting wheel overnight at 4°C. The beads were washed at 4°C with 30mL buffer containing 50 mM HEPES at pH 7.4, 400 mM KCl, 10% glycerol, 1 mM TCEP, and 10 mM Imidazole, then with another 30mL buffer containing 50 mM HEPES at pH 7.4, 400 mM KCl, 10% glycerol, 1 mM TCEP, and 25 mM Imidazole, followed the third 30 mL buffer containing 50 mM HEPES at pH 7.4, 270 mM KCl, 10% glycerol, 1 mM TCEP, and 25 mM Imidazole. 100 µL of PreScission protease (~2 $mg.mL^{-1}$) in 1 mL buffer was added to the beads and incubated for 3 hours at room temperature with shaking to remove the 12xHis tag. After the cleavage reaction, elusions were collected and gel filtrated using a Superdex 200 column. The protein concentration was typically 1 to 2 $mg.mL^{-1}$ as determined by using a Bradford protein assay with Bovine Serum Albumin (BSA) as the standard.

Protein labeling

The Munc13-1-Halo proteins were labeled by incubating the proteins with Alexa488 or Alexa660 conjugated with Halo ligand from Promega, as described before (*13*). The protein was first centrifuged at 14,000 rpm for 20 minutes at 4°C to remove any precipitation. Fluorescence dye was added into the protein solution at dye:protein = 5:1 molar ratio and the mixture was incubated for 30 min at room temperature with gentle rotation. Unreacted dye was removed by passing through the PD MidiTrap G-25 column (GE Healthcare) three times at room temperature. The labeling efficiencies were about 97%.

Liposome formation

Protein-free liposomes were prepared by extrusion using an Avestin mini-extruder (*7, 17*). To make the liposomes for preparing bilayers, DOPC, DOPS, DAG, TopFluor® DAG, $PI(4,5)P_2$, TopFluor® $PI(4,5)P_2$, and/or TopFluor® TMR $PI(4,5)P_2$ were mixed at proper mole ratio. Total amount was 3 µmoles. Nitrogen flow was use to remove the liquid solvents, and lipids were then dried in vacuum for 2 hours, followed by re-suspension with 500 µL buffer containing 50 mM HEPES, 140 mM KCl, and 10% glycerol. The resuspended lipids were treated with freezing (using liquid nitrogen) and thawing (in 37°C water bath) cycles for 8 times, followed by extrusion using 100 nm or 50 nm membrane for 21 times.

We usually had 2% DAG, a reasonable estimate of the physiological DAG level, because it was previously reported that DAG level is around 0.4% to 2% in hepatocytes (*40*). At the plasma

membrane, $PI(4,5)P_2$ is about 0.4 mol% to 4 mol% (*41*), and can be converted to DAG through hydrolysis (*28*). Both $PI(4,5)P_2$ and DAG are able to be enriched to high local concentration in the presence of Syntaxin-1 juxtamembrane domain (*27*).

To make the liposomes for preparing vesicles, 68 mol% DOPC, 30 mol% DOPS, and 2 mol% DOPE-Atto647N were mixed. Total amount was 3 μmoles, and liposomes were produced similarly as above.

Bilayer Preparation and TIRF microscopy

Bilayers were prepared by bursting liposomes on the glass surface using a glass-bottomed μ-Slide $V1^{0.5}$ chip from Ibidi. 2.5 μL $MgCl_2$ at 500 mM were added into 122.5 μL buffer containing 50 mM HEPES (pH 7.4), 140 mM KCl, and 10% glycerol. Then 125 μL extruded bilayer liposomes were added. 60 μL $MgCl_2$-liposome solution were loaded into the channel of the ibidi chip and incubate for 40 min at room temperature. The channel was washed with the same buffer supplemented with 6 mM EDTA, and then with buffer supplemented with 1 mM DTT. Depending on the purpose of experiments, $MgCl_2$ or $CaCl_2$ may be added in the buffer to the desired concentration. 60 μL of 10 nM Munc13-1-Halo-Alexa488 were loaded into the channel and incubate with the bilayer for 60 min at room temperature. The channel was washed with the buffer supplemented with 1 mM DTT. The vesicle liposomes were diluted 30 times. 60 μL diluted vesicle liposomes were loaded into the channel and incubate for 5 min at room temperature. The channel was washed with buffer supplemented with 1 mM DTT.

The Ibidi chip was then mounted to the stage of a Nikon TIRF microscope. Bilayers, Munc13 particles on bilayers, and vesicles attached to bilayers were respectively imaged at room temperature with the TIRF microscope using the corresponding laser.

Counting Munc13 copy numbers

To determine the number of copies of Munc13C in each DAG domain, we gradually bleached the image frames using suitable laser power at different positions. The bleaching profiles (particle fluorescence intensity versus time) were plotted and a variety of bleaching patterns were found. When the Munc13C copy number was small, the bleaching profile displayed apparent discrete steps, and the actual number of proteins can be determined from counting the number

and intensity of steps. This method only works for relatively small copy numbers (generally, 5–6 or fewer) because the bleaching profile becomes smooth when the copy number is large. As an alternative for larger copy numbers, we fitted the intensity profile using:

$$I(t) = I_0 e^{-\frac{t}{\tau}} + B \quad (4)$$

where $I(t)$ is the intensity at time t, I_0 is the initial intensity before bleaching, τ is the decay time constant, and B is the background. Hence, the copy number N can be obtained through

$$N = \frac{I_0}{i} \quad (5)$$

where i is the unit intensity of a single fluorophore, *i.e.* the average intensity of a single bleaching step determined using small clusters.

Mass photometry

Mass photometry experiments were performed an OneMP instrument (Refeyn, Oxford, UK) at room temperature (*42, 43*). The microscope coverslips (24 × 50 mm, Fisher Scientific) and precut 2 × 2 silicon gasket wells (Sigma) were cleaned with MilliQ water, isopropanol, and dried with clean nitrogen flow, and assembled with an adjustable cover-slip rack. The instrument was calibrated using β-Amylase and Thyroglobulin from Refeyn as protein standards: 18 μL of the buffer was added in an empty well on the coverslip and the laser was focused; then 2 μL of β-Amylase or Thyroglobulin was added and mixed by pipetting; data acquisition was started immediately and the MP video was recorded using the AcquireMP software, and then the software DiscoverMP was used to analyze the data and generate the calibration function. To measure the mass of the protein of interest, 10 μL buffer was added to an empty well on the coverslip, then 10 μL of Munc13-1 solution at various concentrations (from 8 nM to 170 nM) was added and well mixed. Data collection was then started and the MP video was recorded. DiscoverMP was used to process the data (*44*). The distribution of molecular mass was plotted as histograms and fit with Gaussian peaks to obtain the average mass of different species and determine the molecular weight of Munc13-1.

Lipid Membrane Preparation for CryoET

Vesicles (DOPC/DOPS/PI(4,5)P_2 in a molar ratio of 14/80/6) were prepared as described previously (*1*). Briefly, the lipid stocks were mixed in a chloroform with addition of 20 μL

methanol to dissolve PI(4,5)P_2 and the solvent was evaporated under N_2 gas followed by vacuum drying for 1 h. The dried lipid film was rehydrated for 1 h at room temperature with constant vortexing in buffer containing 20 mM MOPS pH 7.4, 150 mM KCl, 1 mM EDTA, and 0.5 mM TCEP at a final lipid concentration of 1 mM. Next, the mixture was sonicated for 5 min using a bath sonicator (Branson Ultrasonics). Vesicles were used for crystallization next day after storage at 4^{o}C to sediment large lipid aggregates.

Protein Crystallization for CryoET

Vesicles were diluted down to lipid concentration of 100 μM and mixed with 1 μM Munc13C protein in 1:1 (vol/vol) ratio. Once mixed, the samples were incubated at room temperature for 5 min then kept on ice until freezing.

Electron Microscopy Sample Preparation and Data Acquisition

Samples (2.5 μL) were vitrified using a Vitrobot Mark IV (Thermo Fisher Scientific) held at 8^{o}C with 100% humidity. They were applied to freshly glow-discharged 200 mesh Lacey Formvar/carbon grids and grids were blotted for 5 s with blot force -1 and then plunged frozen in liquid ethane cooled by liquid nitrogen. Samples with wild-type protein were imaged using Glacios Cryo TEM 200 kV (Thermo Fisher Scientific) equipped with a K2 Summit direct electron detector (Gatan). The K2 camera was used in counting mode, and detector dark and gain references were collected prior to each data acquisition session. The tilt-series movies were acquired using SerialEM with a bidirectional scheme starting from +20°; -43 to +44° tilt range with 3° increment, 80 e/A2 total dose. The nominal magnification was 13,500× resulting in a pixel size of 3.02 Å. Nominal defocus was set to -4.5 μm. Quadruple mutant tilt-series were collected using a 300 kV Titan Krios G2 transmission electron microscope (Thermo Fisher Scientific) equipped with GIF Quantum LS energy filter and K3 Summit direct electron detector (Gatan). The slit width of the filter was set to 20 eV. Filter tuning was done using Digital Micrograph software (Gatan). The tilt-series movies were acquired using SerialEM at a nominal magnification of 42,000× (corresponding to a calibrated physical pixel size of 2.1 Å) using dose symmetric scheme (*45*) with tilt range ± 51° and 3° increment. The tilt images were acquired as 11,520 × 8,184 super-resolution movies of 10 frames per each tilt corresponding to a tilt series total dose ∼120 e/Å2, respectively. Nominal defocus was set to -5 μm. Movies were aligned and

saved as mrc stacks using alignframes from IMOD package (*46*). The resulting tilt series were aligned and reconstructed with 4x binning for and 8x binning by AreTomo (*47*) so the final pixel size of reconstructed tomograms was 12.08 Å and 16.8 Å. Topaz denoising was used to denoise selected tomograms using unet-3d-20a pretrained model (*48*).

SUPPORTING INFORMATION

Supporting Information includes: Supporting Text, Supporting Table, and Supporting Figures.

AUTHOR CONTRIBUTIONS

F.L., F.P. and J.E.R designed research; F.L., J.C. and K.G. performed research; F.L., F.P. and J.E.R. analyzed data; and F.L., F.P. and J.E.R wrote the paper.

ACKNOWLEDGMENTS

This work was supported by National Institute of Health (NIH) grant DK027044 to JER.

REFERENCES

1. K. Grushin, R. V. Kalyana Sundaram, C. V. Sindelar, J. E. Rothman, Munc13 structural transitions and oligomers that may choreograph successive stages in vesicle priming for neurotransmitter release. *Proceedings of the National Academy of Sciences of the United States of America* **119**, (2022).
2. K. Hashimoto, A. R. Panchenko, Mechanisms of protein oligomerization, the critical role of insertions and deletions in maintaining different oligomeric states. *Proceedings of the National Academy of Sciences of the United States of America* **107**, 20352-20357 (2010).
3. S. E. Ahnert, J. A. Marsh, H. Hernandez, C. V. Robinson, S. A. Teichmann, Principles of assembly reveal a periodic table of protein complexes. *Science* **350**, aaa2245 (2015).
4. J. A. Marsh, S. A. Teichmann, Structure, dynamics, assembly, and evolution of protein complexes. *Annual review of biochemistry* **84**, 551-575 (2015).
5. A. Betz *et al.*, Munc13-1 is a presynaptic phorbol ester receptor that enhances neurotransmitter release. *Neuron* **21**, 123-136 (1998).
6. I. Augustin, C. Rosenmund, T. C. Sudhof, N. Brose, Munc13-1 is essential for fusion competence of glutamatergic synaptic vesicles. *Nature* **400**, 457-461 (1999).
7. F. Li *et al.*, A Half-Zippered SNARE Complex Represents a Functional Intermediate in Membrane Fusion. *Journal of the American Chemical Society* **136**, 3456-3464 (2014).

8. J. Xu *et al.*, Mechanistic insights into neurotransmitter release and presynaptic plasticity from the crystal structure of Munc13-1 C1C2BMUN. *Elife* **6**, (2017).
9. M. Camacho *et al.*, Heterodimerization of Munc13 C2A domain with RIM regulates synaptic vesicle docking and priming. *Nature communications* **8**, 15293 (2017).
10. X. Liu *et al.*, Functional synergy between the Munc13 C-terminal C1 and C2 domains. *Elife* **5**, (2016).
11. Y. Lai *et al.*, Molecular Mechanisms of Synaptic Vesicle Priming by Munc13 and Munc18. *Neuron* **95**, 591-607 e510 (2017).
12. M. Padmanarayana *et al.*, A unique C2 domain at the C terminus of Munc13 promotes synaptic vesicle priming. *Proceedings of the National Academy of Sciences of the United States of America* **118**, (2021).
13. F. Li, N. Tiwari, J. E. Rothman, F. Pincet, Kinetic barriers to SNAREpin assembly in the regulation of membrane docking/priming and fusion. *Proceedings of the National Academy of Sciences of the United States of America* **113**, 10536-10541 (2016).
14. Q. Zhou *et al.*, The primed SNARE-complexin-synaptotagmin complex for neuronal exocytosis. *Nature* **548**, 420-425 (2017).
15. J. E. Rothman, K. Grushin, M. Bera, F. Pincet, Turbocharging synaptic transmission. *FEBS letters*, (2023).
16. B. Quade *et al.*, Membrane bridging by Munc13-1 is crucial for neurotransmitter release. *Elife* **8**, (2019).
17. F. Li *et al.*, Vesicle capture by membrane-bound Munc13-1 requires self-assembly into discrete clusters. *FEBS letters* **595**, 2185-2196 (2021).
18. S. Wang *et al.*, Conformational change of syntaxin linker region induced by Munc13s initiates SNARE complex formation in synaptic exocytosis. *The EMBO journal* **36**, 816-829 (2017).
19. R. V. Kalyana Sundaram *et al.*, Munc13 binds and recruits SNAP25 to chaperone SNARE complex assembly. *FEBS letters* **595**, 297-309 (2021).
20. S. Wang *et al.*, Munc18 and Munc13 serve as a functional template to orchestrate neuronal SNARE complex assembly. *Nature communications* **10**, 69 (2019).
21. H. Sakamoto *et al.*, Synaptic weight set by Munc13-1 supramolecular assemblies. *Nature neuroscience* **21**, 41-49 (2018).
22. T. A. Ryan, Munc13 marks the spot. *Nature neuroscience* **21**, 5-6 (2018).
23. A. Radhakrishnan *et al.*, Symmetrical arrangement of proteins under release-ready vesicles in presynaptic terminals. *Proceedings of the National Academy of Sciences of the United States of America* **118**, (2021).
24. X. Li *et al.*, Symmetrical organization of proteins under docked synaptic vesicles. *FEBS letters* **593**, 144-153 (2019).
25. R. V. K. Sundaram *et al.*, Novel Roles for Diacylglycerol in Synaptic Vesicle Priming and Release Revealed by Complete Reconstitution of Core Protein Machinery. *bioRxiv*, (2023).
26. M. Bera *et al.*, Two successive oligomeric Munc13 assemblies scaffold vesicle docking and SNARE assembly to support neurotransmitter release. *bioRxiv*, (2023).
27. A. Honigmann *et al.*, Phosphatidylinositol 4,5-bisphosphate clusters act as molecular beacons for vesicle recruitment. *Nature structural & molecular biology* **20**, 679-686 (2013).
28. B. H. Falkenburger, E. J. Dickson, B. Hille, Quantitative properties and receptor reserve of the DAG and PKC branch of G(q)-coupled receptor signaling. *J Gen Physiol* **141**, 537-555 (2013).
29. M. W. Lee, D. L. Severson, Signal transduction in vascular smooth muscle: diacylglycerol second messengers and PKC action. *Am J Physiol* **267**, C659-678 (1994).
30. M. J. Berridge, Inositol trisphosphate and diacylglycerol: two interacting second messengers. *Annual review of biochemistry* **56**, 159-193 (1987).

31. S. Leikin, M. M. Kozlov, N. L. Fuller, R. P. Rand, Measured effects of diacylglycerol on structural and elastic properties of phospholipid membranes. *Biophys J* **71**, 2623-2632 (1996).
32. P. Campomanes, V. Zoni, S. Vanni, Local accumulation of diacylglycerol alters membrane properties nonlinearly due to its transbilayer activity. *Commun Chem* **2**, (2019).
33. J. P. Zewe *et al.*, Probing the subcellular distribution of phosphatidylinositol reveals a surprising lack at the plasma membrane. *The Journal of cell biology* **219**, (2020).
34. D. Milovanovic, Y. Wu, X. Bian, P. De Camilli, A liquid phase of synapsin and lipid vesicles. *Science* **361**, 604-607 (2018).
35. X. Wu *et al.*, Vesicle Tethering on the Surface of Phase-Separated Active Zone Condensates. *Mol Cell* **81**, 13-24 e17 (2021).
36. X. Yang *et al.*, Syntaxin opening by the MUN domain underlies the function of Munc13 in synaptic-vesicle priming. *Nature structural & molecular biology* **22**, 547-554 (2015).
37. F. Parlati *et al.*, Rapid and efficient fusion of phospholipid vesicles by the alpha-helical core of a SNARE complex in the absence of an N-terminal regulatory domain. *Proceedings of the National Academy of Sciences of the United States of America* **96**, 12565-12570 (1999).
38. H. Ji *et al.*, Protein determinants of SNARE-mediated lipid mixing. *Biophys J* **99**, 553-560 (2010).
39. T. J. Melia *et al.*, Regulation of membrane fusion by the membrane-proximal coil of the t-SNARE during zippering of SNAREpins. *The Journal of cell biology* **158**, 929-940 (2002).
40. J. Preiss *et al.*, Quantitative measurement of sn-1,2-diacylglycerols present in platelets, hepatocytes, and ras- and sis-transformed normal rat kidney cells. *The Journal of biological chemistry* **261**, 8597-8600 (1986).
41. R. C. Wills, G. R. V. Hammond, PI(4,5)P2: signaling the plasma membrane. *Biochem J* **479**, 2311-2325 (2022).
42. D. Wu, G. Piszczek, Standard protocol for mass photometry experiments. *Eur Biophys J* **50**, 403-409 (2021).
43. Z. Rashidijahanabad *et al.*, Virus-like Particle Display of Vibrio choleraeO-Specific Polysaccharide as a Potential Vaccine against Cholera. *ACS Infect Dis* **8**, 574-583 (2022).
44. S. Niebling *et al.*, Biophysical Screening Pipeline for Cryo-EM Grid Preparation of Membrane Proteins. *Front Mol Biosci* **9**, 882288 (2022).
45. W. J. H. Hagen, W. Wan, J. A. G. Briggs, Implementation of a cryo-electron tomography tilt-scheme optimized for high resolution subtomogram averaging. *J Struct Biol* **197**, 191-198 (2017).
46. J. R. Kremer, D. N. Mastronarde, J. R. McIntosh, Computer visualization of three-dimensional image data using IMOD. *J Struct Biol* **116**, 71-76 (1996).
47. S. Zheng *et al.*, AreTomo: An integrated software package for automated marker-free, motion-corrected cryo-electron tomographic alignment and reconstruction. *J Struct Biol X* **6**, 100068 (2022).
48. T. Bepler, K. Kelley, A. J. Noble, B. Berger, Topaz-Denoise: general deep denoising models for cryoEM and cryoET. *Nature communications* **11**, 5208 (2020).

FIGURE LEGENDS

Figure 1. DAG forms microdomains on lipid bilayer, and wildtype Munc13-1 clusters are located at these microdomains. (**A**) to (**C**) Representative TIRF images of fluorescent DAG in bilayers and Munc13-1 bound to bilayers: (**A**) bilayer with 2% TopFluor® DAG, 0% non-fluorescent DAG, and 2% non-fluorescent $PI(4,5)P_2$; (**B**) bilayer with 2% TopFluor® DAG, 3% non-fluorescent DAG, and 2% non-fluorescent $PI(4,5)P_2$; and (**C**) bilayer with 2% TopFluor® DAG, 8% non-fluorescent DAG, and 2% non-fluorescent $PI(4,5)P_2$. Left panels are fluorescent DAG, the middle panels are Munc13-1 labeled with Alexa 660, and right panels are the merge the previous two panels. (**D**) Representative TIRF images of fluorescent $PI(4,5)P_2$ in bilayers which contains 2% non-fluorescent DAG and 2% TopFluor® $PI(4,5)P_2$. Left panel is fluorescent $PI(4,5)P_2$, the middle panel is Munc13-1 labeled with Alexa 660, and right panels are the merge the previous two panels. (**E**) Distributions of the copy number of Munc13-1 molecules in the clusters with various DAG amounts (sample size: $n = 4$ for 2% Top-Fluor DAG; $n = 3$ for 2% Top-Fluor DAG + 3% DAG; and $n = 5$ for 2% DAG,); and (**F**) Distribution of the area of DAG microdomains (sample size: $n = 4$ for2% Top-Fluor DAG; $n = 3$ for 2% Top-Fluor DAG + 3% DAG; and $n = 3$ for 2%bTop-Fluor DAG + 8% DAG). (**G**) The molecular weight of Munc13C-Halo-Alexa 660 in solution was measured with Mass Photometer. Final concentration of Munc13C-Halo-Alexa 660 in this measurement was around 10 nM. The experimental molecular mass nearly equals to its theoretical molecular weight.

Figure 2. Poisson distribution modeling of oligomers in wildtype Munc13-1 clusters. (**A**) Single Poisson distribution, assuming all wildtype Munc13-1 in monomer state; (**B**) through (**D**) Dual Poisson distribution (monomer + uniform size oligomer), 2-step process: monomer with pentamer (**B**), monomer with hexamer (**C**), and monomer with heptamer (**D**). The orange bars represent predicted distribution of the copy number of Munc13-1 molecules in the clusters, and the green dashed lines are experimental data (sample size $n = 5$). (**E**) The O value of the Poisson modelling as function of the assumed oligomeric state of wildtype Munc13-1. Larger O value suggests the predicted oligomeric state fits better with observed data.

Figure 3. Mutations in interaction interface between C_2C and neighboring MUN domain in the Munc13-1 hexagon affect the protein organization, cluster size distribution, and vesicle capture. (**A**) Top and side views of the hexagonal cage of Munc13-1 oligomer that binds a vesicle (based on PDB 7T7C). C_2C domains are colored in purple, MUN domains in grey and C_2B in blue. The red rectangular area shows the position of interaction interface between C_2C and MUN domain in Munc13-1 hexagon. (**B**) Close-up view of interface in ribbon representation. Possibly involved residues in interaction are labeled. The interface contains two

669 separate regions: hydrophobic (green colored amino acid residues) and polar (red and blue
670 colored amino acid residues). (**C**) and (**D**) Slices through the reconstructed tomograms. (**C**) Wild
671 type Munc13C hexagonal crystal between negatively charged lipid bilayers. Top panel is the
672 Topaz-denoised (*48*) top view of the crystal. Bottom is the side view of the crystal with visible
673 protein density lane in the middle between lipid bilayers corresponding to the top of hexagons
674 (**A**) formed by lateral conformation of Munc13-1. (**D**) Top panel is the Topaz-denoised top view
675 of the crystal formed by F1176N/I1215N/E1139R/D1039R Munc13-1 mutant. This crystal is
676 characterized as a rectangular lattice with denser protein packing in form of rows of
677 round-shaped densities and protein-filled space between them. Lower panel is the slice through
678 the side of the crystal. The middle protein density lane is no longer visible. Scale bars 50 nm.
679 (**E**) Overlay of TIRF image of Munc13-1 interface mutant labeled with Alexa 488 on lipid
680 bilayer membrane containing PC, PS, DAG, and PI(4,5)P_2, with TIRF image of captured vesicles
681 by the same Munc13-1 interface mutant (vesicles labeled with Atto647N, pink). (**F**) Distribution
682 of the copy number of Munc13-1 interface mutant molecules in the clusters (purple columns)
683 (sample size $n = 4$). The green dots represent the distribution of the copy number in the clusters
684 formed by wildtype Munc13-1, which serves as a reference. (**G**) The *O* value of the Poisson
685 modelling as function of the assumed oligomeric state of the Munc13-1 interface mutant (purple
686 solid line). The green dashed line represent the *O* value of wildtype Munc13-1 clusters, which
687 serves as a reference (**H**) Probability of vesicle capture by the clusters of Munc13-1 interface
688 mutant (purple columns) as a function of their cluster size which is the copy number of the
689 protein molecules in the cluster (sample size $n = 4$). The green dashed line represent the
690 probability of wildtype Munc13-1 clusters, which serves as a reference.

691

692 **Figure 4. DAG plays a critical role in wildtype Munc13-1's function of vesicle capture.**
693 (**A**) Overlay of TIRF image of wildtype Munc13-1 clusters formed on a bilayer with 2% DAG
694 (wildtype Munc13-1 labeled with Alexa488, green) with TIRF image of captured vesicles
695 (vesicles labeled with Atto647N, pink). (**B**) Overlay of TIRF image of wildtype Munc13-1
696 clusters that were formed on bilayer in the absence of any DAG (Munc13-1, green) with vesicles
697 bound to the same bilayer (vesicles, pink). (**C**) Distribution of the copy number of wildtype
698 Munc13-1 molecules in the clusters on lipid bilayer in the presence of DAG that are capable
699 (orange) and incapable (blue) of capturing vesicle, respectively (sample size $n = 5$). (**D**)
700 Distribution of the copy number of wild-type Munc13-1 molecules in the clusters on lipid bilayer
701 in the absence of DAG that are capable (orange) and incapable (blue) of capturing vesicle,
702 respectively (sample size $n = 4$).

703

704 **Figure 5. Quantal relationship of the number of captured vesicles by a cluster and the**
705 **number of copies of Munc13-1 molecules in the same cluster.** (**A**) & (**B**) Qualitative

correlation between optical cluster sizes and the optical sizes of captured vesicles. When the intensities of Munc13-1 clusters (**A**) are bigger, the corresponding intensities of captured vesicles (**B**) are larger. (**C**) Intensity distribution of captured vesicles as a function of the copy numbers of Munc13-1 molecules in the corresponding clusters shows three distinct regimes. Different symbols and colors represent the data points were from different independent experiments, sample size $n = 5$. (**D**) Comparison of predicted number of captured vesicle as a function of the copy number of Munc13-1 molecules in the cluster (black squares), and experimental average number of captured vesicles that was determined from vesicle intensities, versus the copy number of Munc13-1 molecules in the cluster (red spheres).

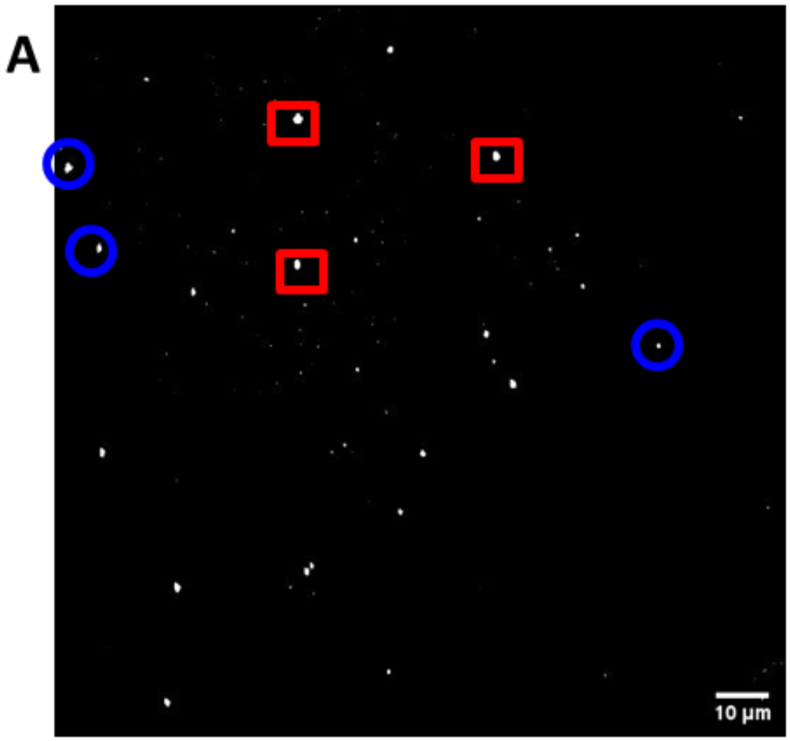
A
10 µm

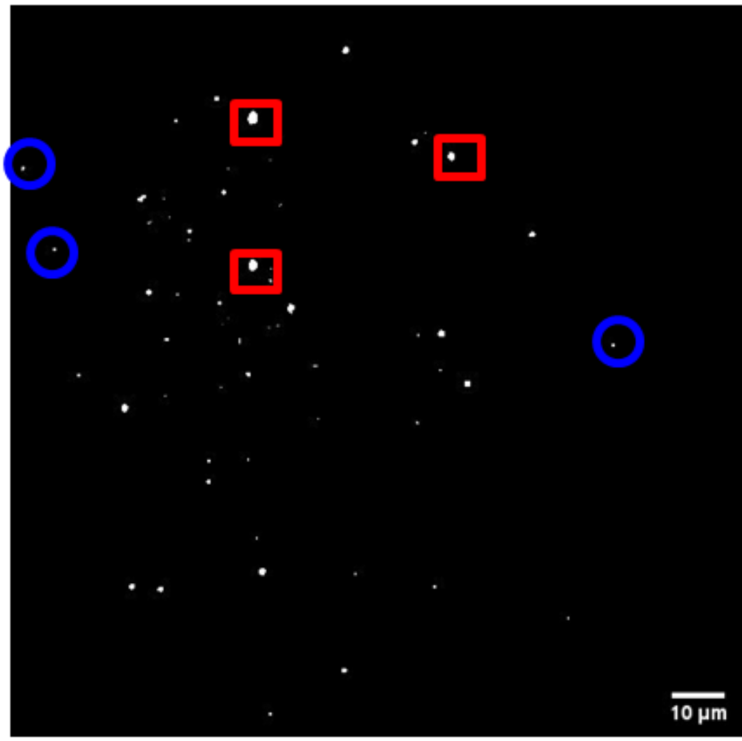
B
10 µm

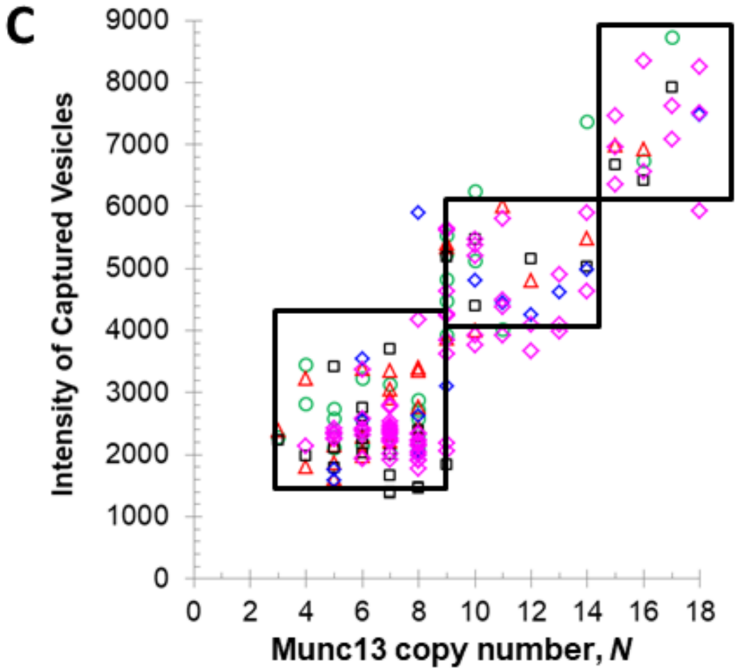
C
Intensity of Captured Vesicles
9000
8000
7000
6000
5000
4000
3000
2000
1000
0
0
2
4
6
8
10
12
14
16
18
Munc13 copy number, N

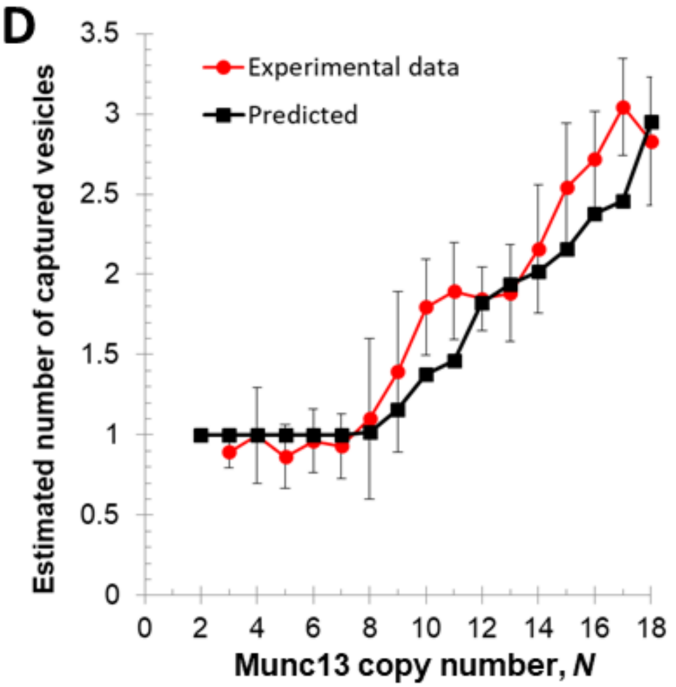
D
Estimated number of captured vesicles
3.5
3
2.5
2
1.5
1
0.5
0
Experimental data
Predicted
0
2
4
6
8
10
12
14
16
18
Munc13 copy number, N

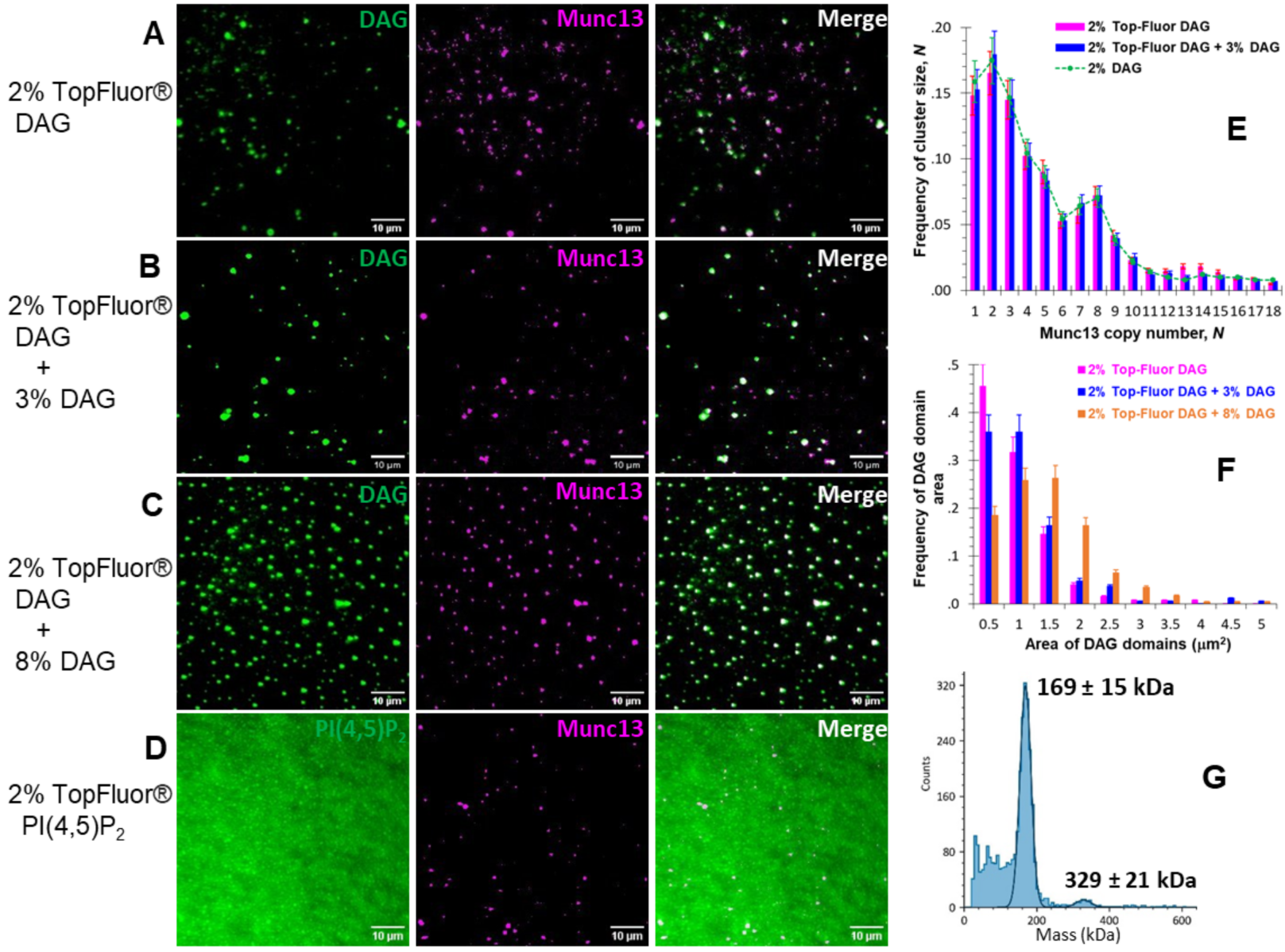
A
2% TopFluor® DAG
DAG
Munc13
Merge
B
2% TopFluor® DAG + 3% DAG
C
2% TopFluor® DAG + 8% DAG
D
2% TopFluor® PI(4,5)P2
PI(4,5)P2
10 µm
E
2% Top-Fluor DAG
2% Top-Fluor DAG + 3% DAG
2% DAG
Frequency of cluster size, N
Munc13 copy number, N
F
2% Top-Fluor DAG + 8% DAG
Frequency of DAG domain area
Area of DAG domains (µm²)
G
169 ± 15 kDa
329 ± 21 kDa
Counts
Mass (kDa)

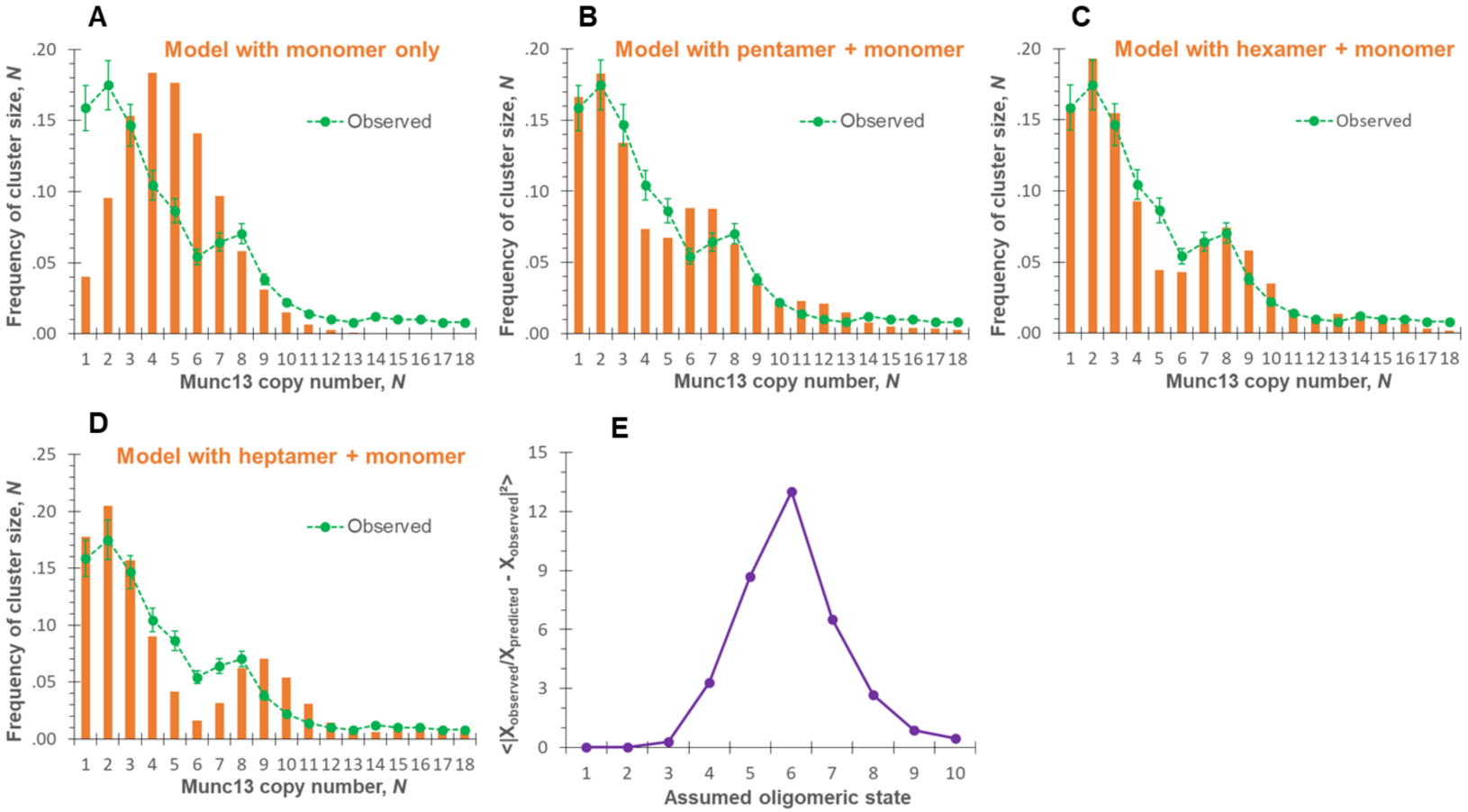
A
Model with monomer only
Observed
Frequency of cluster size, N
Munc13 copy number, N
B
Model with pentamer + monomer
Observed
Frequency of cluster size, N
Munc13 copy number, N
C
Model with hexamer + monomer
Observed
Frequency of cluster size, N
Munc13 copy number, N
D
Model with heptamer + monomer
Observed
Frequency of cluster size, N
Munc13 copy number, N
E
<|X observed/X predicted - X observed|2>
Assumed oligomeric state

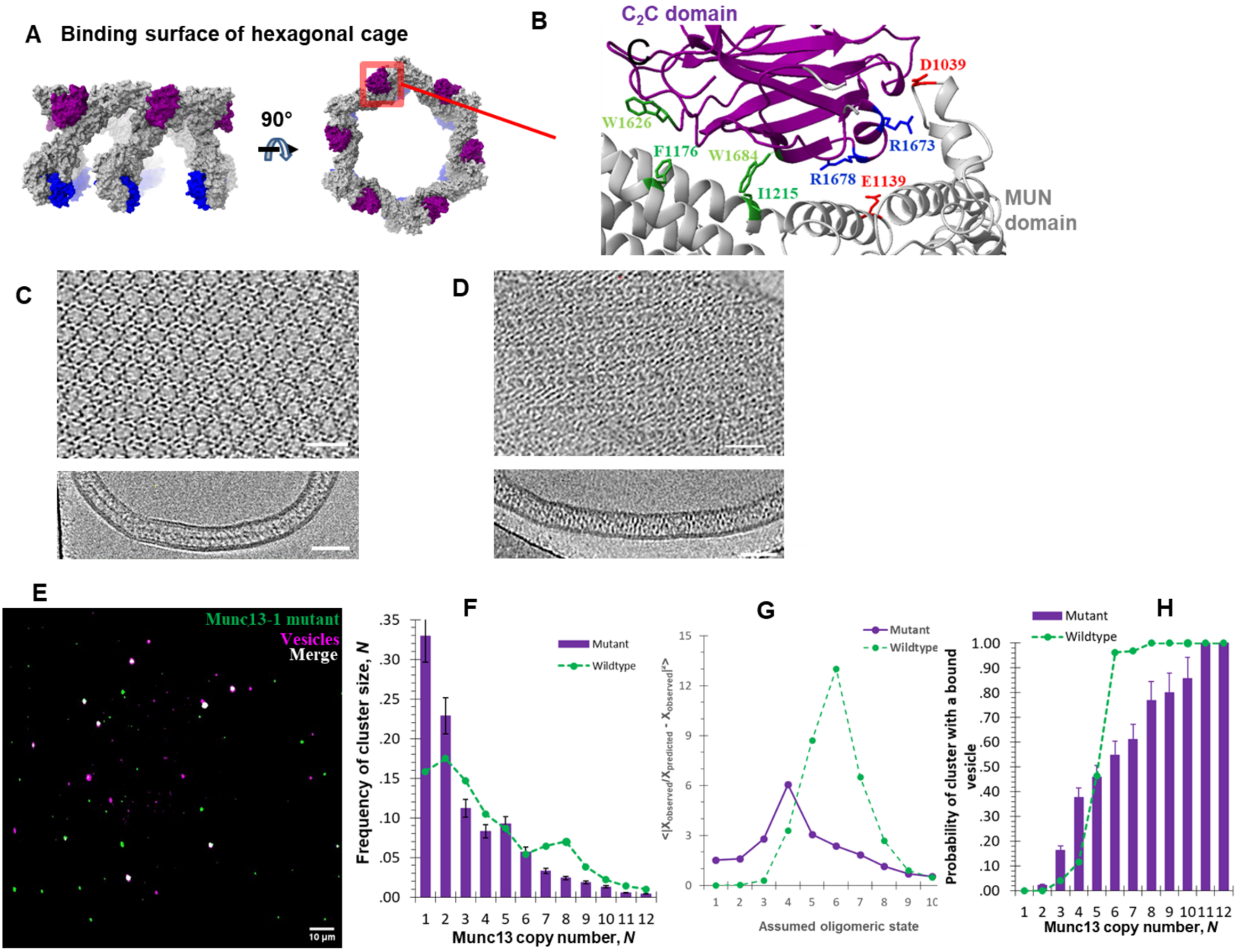
A
Binding surface of hexagonal cage
90°
B
C2C domain
C
D1039
W1626
R1673
F1176
W1684
R1678
E1139
I1215
MUN domain
C
D
E
Munc13-1 mutant
Vesicles
Merge
10 µm
F
Frequency of cluster size, N
Mutant
Wildtype
Munc13 copy number, N
G
Mutant
Wildtype
Assumed oligomeric state
H
Mutant
Wildtype
Probability of cluster with a bound vesicle
Munc13 copy number, N

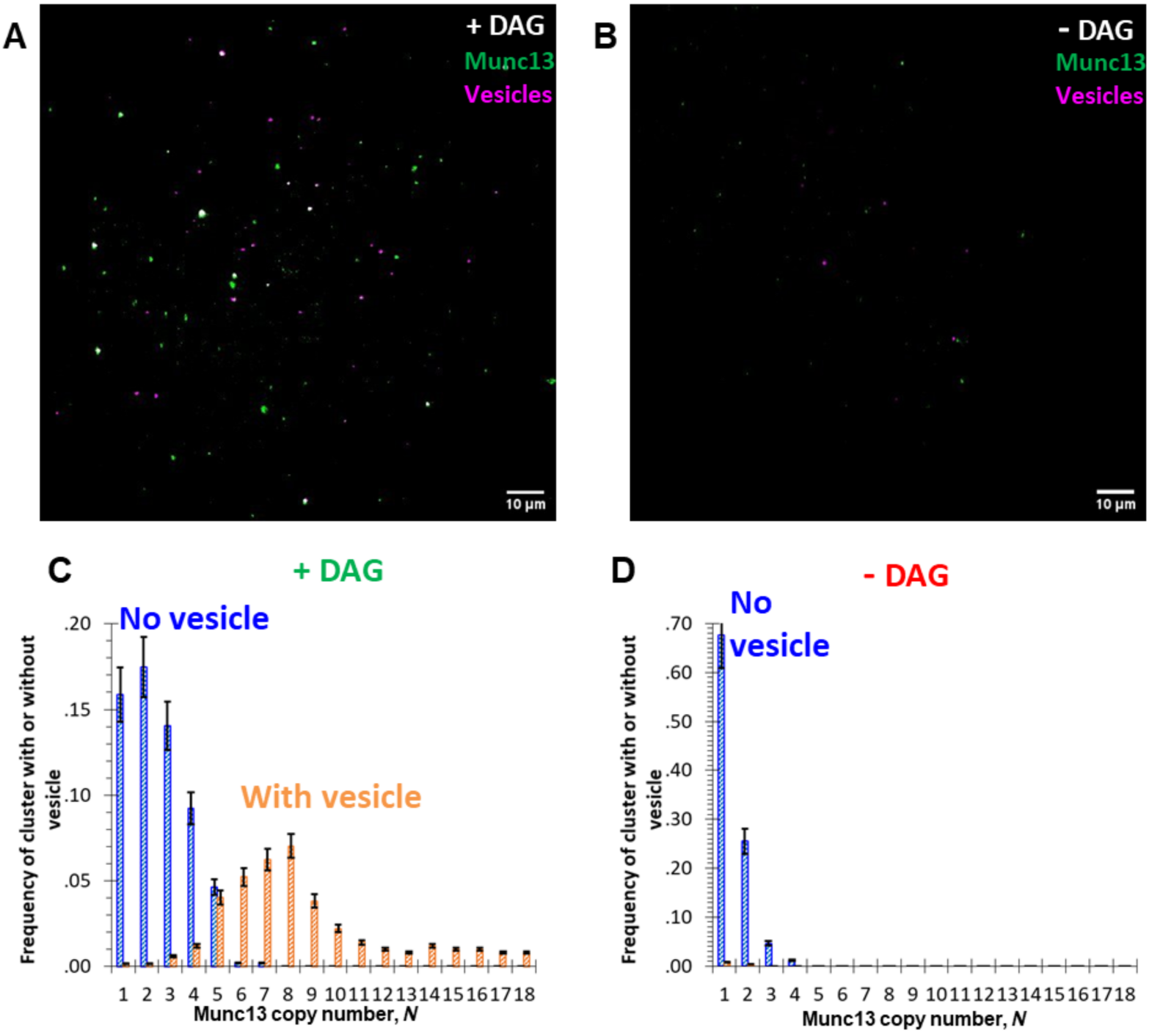
A
+ DAG
Munc13
Vesicles
10 µm
B
- DAG
Munc13
Vesicles
10 µm
C
+ DAG
No vesicle
With vesicle
Frequency of cluster with or without vesicle
.00
.05
.10
.15
.20
1 2 3 4 5 6 7 8 9 10 11 12 13 14 15 16 17 18
Munc13 copy number, N
D
- DAG
No vesicle
Frequency of cluster with or without vesicle
.00
.10
.20
.30
.40
.50
.60
.70
1 2 3 4 5 6 7 8 9 10 11 12 13 14 15 16 17 18
Munc13 copy number, N